Contributions to Hadron Therapy Using Laser-Plasma Accelerators

Summary

Doctorand: Mircea Patrascoiu

Coordonator Stiintific: CS 1 Dr. Catalin M. Ticos

1. Introduction and Research Problem

Hadron therapy is based on the therapeutic use of charged particles, most often protons and carbon ions, whose physical interaction with matter makes it possible to concentrate dose inside the tumour volume while reducing unnecessary irradiation of healthy tissue. Its clinical advantage is connected to the Bragg peak: charged particles deposit a relatively moderate dose at the entrance, release most of their energy near the end of their range, and then stop. By selecting the particle energy, the maximum dose can be placed at a chosen depth, while a spread-out Bragg peak can be constructed to cover a finite tumour thickness. This depth selectivity is the reason hadron therapy remains one of the most advanced forms of radiotherapy. [1-7]

The medical value of hadron therapy is already established, but its practical expansion is limited by the size, complexity, and cost of conventional accelerator facilities. Cyclotrons can deliver stable high-energy proton beams, but their fixed extraction energy requires degraders and additional downstream systems for range control. Synchrotrons allow direct variation of the extracted energy, but they are larger, more complex, and expensive to build and operate. In both cases, the accelerator is only one part of the full treatment system. The facility also requires beam transport lines, energy selection, beam diagnostics, patient-specific delivery systems, shielding, and in many cases heavy rotating gantries. [1-5]

The beam delivery system is a central engineering constraint. Passive scattering can broaden and modulate the beam, but it introduces additional secondary radiation and patient-specific hardware. Pencil beam scanning improves conformity by magnetically steering a narrow beam spot through the target volume layer by layer. Modern proton and ion therapy therefore depends not only on reaching the required energy, but also on preserving beam position, divergence, spot size, and energy control at the treatment point. Rotating gantries make this more demanding because the optical quality of the beam must be maintained while the beamline changes angle around the patient. For carbon ions, the higher magnetic rigidity makes gantries even larger and more difficult to compact. [8-9]

Laser-plasma acceleration offers a different route toward charged-particle beam generation. Instead of accelerating particles over metres or hundreds of metres in radio-frequency structures, an ultra-intense laser pulse can transfer energy to a plasma over micrometre-to-millimetre interaction lengths. Petawatt-class lasers can produce electric fields far beyond those available in conventional accelerators, which makes them attractive as compact sources for future medical physics and radiobiology applications. Facilities such as ELI-NP demonstrate that multi-petawatt laser systems are now mature enough to support high-intensity laser-target experiments, secondary particle generation, and beamline-development studies. [10-17]

The compactness of the acceleration mechanism does not by itself create a clinical beam. Laser-driven ion sources have properties that are almost opposite to those of conventional medical accelerators. They produce short particle bunches with very high instantaneous dose rate, but the raw beam is broad in energy, strongly divergent, mixed in particle species, and sensitive to laser-target conditions. Protons, carbon ions, helium ions, electrons, photons, and target contaminants may emerge together. A useful medical or radiobiological beam therefore requires capture, energy selection, particle filtering, collimation, focusing, and dosimetry before it can be delivered to a target. [10, 16-19]

The central problem addressed here is the transformation of a compact but non-ideal laser-plasma source into a controlled beamline suitable for hadron-therapy-related research. The work does not assume that a laser-driven source can be placed directly in front of a patient or biological sample. Instead, it treats the source as the beginning of a transport problem. The beamline must accept the useful part of a large-divergence distribution, select an energy interval relevant to particle penetration, reject unwanted species, reduce the transverse beam size, and preserve a sufficient number of particles for irradiation. [10, 18-19]

The research objective is therefore to investigate compact magnetic transport systems capable of conditioning laser-driven proton and ion beams. The study combines theoretical beam physics, magnet design, electromagnetic simulation, and charged-particle tracking. It examines the role of dipoles, quadrupoles, and solenoids in energy selection and focusing, first in a proton steering concept and then in a more complete carbon-ion transport line. The result is a specification-level evaluation of whether realistic magnetic components can capture, select, and refocus a laser-driven ion population in an energy interval relevant to hadron therapy research. [10, 18-19]

2. Laser-Plasma Sources and Medical Relevance

The main laser-driven acceleration mechanism considered as a source model is Target Normal Sheath Acceleration. In this regime, an ultra-intense laser pulse irradiates a thin solid target and creates a population of hot electrons at the front surface. These electrons are driven through the target and emerge at the rear surface, where they generate a strong electrostatic sheath field. Hydrogen-rich contaminants on the rear surface are ionized and accelerated normal to the target. Because protons have a favourable charge-to-mass ratio, they are often accelerated efficiently, while heavier ions such as carbon or helium can also be produced from the target material or from controlled layers. [15-17, 20]

TNSA beams are compact and intense, but they are not monoenergetic. The particle spectrum is generally broad and approximately exponential, with many particles at lower energy and fewer at the high-energy end. Proton energies from a few MeV to several tens of MeV are common in many experiments, while optimized petawatt and multi-petawatt conditions can push the maximum energy higher. Heavy ions are more difficult to accelerate to the same energy per nucleon because of their mass, charge-state dynamics, and stronger sensitivity to target conditions. For carbon ions, energies relevant to deep clinical therapy remain challenging, although intermediate energies are already useful for beamline development, detector testing, and radiobiology. [4-5, 11-14, 16-17, 20]

Other acceleration regimes are relevant because they point toward improved beam quality. Radiation Pressure Acceleration uses the direct momentum transfer from the laser to the plasma surface. In the light-sail limit, an ultrathin target can be pushed collectively, which may produce narrower spectra than TNSA. Break-Out Afterburner acceleration occurs when an ultrathin target becomes relativistically transparent and the laser continues to drive ions inside the target volume. These regimes can in principle reach higher ion energies and better spectral structure, but they require excellent laser contrast, very thin targets, and control of plasma instabilities. For this reason, they remain important research directions rather than routine medical sources. [17, 21-24]

Petawatt-class lasers are relevant because therapy-scale proton and ion energies require extremely high intensities and stable operation. Chirped pulse amplification made such lasers possible by stretching, amplifying, and recompressing short pulses to avoid damage to optical components. Modern facilities now support laser-plasma acceleration, high-energy-density physics, radiation source development, and radiobiology. ELI-NP, with two 10 PW arms, is especially significant for experiments that connect high-intensity laser physics with nuclear physics and possible medical applications. [11-14]

The medical interest in laser-driven beams is strengthened by the emergence of FLASH radiotherapy. FLASH refers to the delivery of radiation at ultra-high dose rates, typically above 40 Gy/s, over very short irradiation times. Preclinical work suggests that under selected conditions this temporal structure can reduce normal-tissue damage while preserving tumour control. The mechanisms remain under study and may involve oxygen depletion, reactive oxygen species, vascular effects, and DNA repair dynamics. Laser-driven sources are naturally attractive in this context because their particle bunches can last from picoseconds to nanoseconds, giving extremely high instantaneous dose rates. [16-17, 25-31]

Actual clinical FLASH experience has so far been obtained with modified conventional accelerator systems, not with laser-driven hadron beams. The first reported human FLASH treatment used electrons in a superficial case, and later proton FLASH trials demonstrated feasibility in selected bone-metastasis indications. These studies are important because they show that ultra-high-dose-rate radiotherapy can move into human treatment protocols. They do not, however, prove that laser-driven particles are clinically mature. Laser-driven proton and ion beams remain preclinical and require major advances in source stability, energy control, beam transport, dosimetry, and repetition-rate operation. [31-34]

Radiobiological studies with laser-accelerated protons have nevertheless shown that such beams can produce measurable biological effects when dose is controlled. In vitro experiments have reported dose-dependent tumour-cell damage, and some studies suggest that ultra-short delivery may influence cell response depending on repair pathway status. In vivo and developmental models have been used to study normal-tissue response under ultra-high-dose-rate conditions. These results support the relevance of laser-driven beams for radiobiology, but they also emphasize that interpretation depends strongly on accurate dosimetry, repeatability, pulse structure, and beam characterization. [29-30, 35-39]

The biological relevance of protons and carbon ions also depends on their interaction with tissue. Charged particles lose energy mainly through ionization and excitation of atomic electrons. The stopping power rises as the particle slows down, producing the Bragg peak. Carbon ions deposit energy more densely than protons and can produce higher linear energy transfer and higher relative biological effectiveness. Their Bragg peak is sharper, and their dense ionization tracks can be useful for radioresistant tumours. At the same time, carbon ions require higher energy per nucleon for comparable range and are harder to transport because their magnetic rigidity is higher. [2-7, 40-42]

Laser-driven hadron therapy therefore sits at the intersection of two demanding requirements. The source must eventually reach appropriate particle energies and high shot-to-shot reproducibility, while the transport line must convert a broad, divergent, multi-species distribution into a spatially controlled and energy-selected beam. The present work focuses on the second requirement. It asks whether magnetic systems of realistic size and field strength can capture the useful core of a laser-driven beam and deliver it in a form that is meaningful for radiobiology-scale irradiation. [10, 18-19]

3. Magnetic Transport Framework

The motion of charged particles in a beamline is governed by the Lorentz force. In the magnetic elements considered here, the magnetic component is dominant, so the force is perpendicular to the particle velocity and changes the direction of motion rather than the kinetic energy. This is the foundation of beam steering and focusing. A uniform transverse magnetic field bends a particle along a curved trajectory, while a magnetic field gradient or an axial field can focus the distribution. The amount of bending or focusing depends on particle momentum, charge, field strength, and effective magnetic length. [40-41, 43]

Magnetic rigidity is the key quantity for comparing particles and designing magnets. It expresses the resistance of a particle to magnetic deflection and is equal to momentum divided by charge. A particle with higher rigidity requires either stronger fields or longer magnets to achieve the same bend or focusing strength. Therapeutic protons already require careful relativistic treatment at 70-250 MeV, and carbon ions are more demanding because their momentum at a given energy per nucleon is higher. This is why a transport system suitable for protons cannot automatically be transferred to carbon ions. [4-5, 40-43]

Dipole magnets provide the main tool for steering and energy selection. In a uniform dipole field, particles with different momenta follow trajectories with different radii. A broad energy spectrum therefore becomes spatially separated downstream of the magnet. A slit or aperture placed at an appropriate dispersive plane can select a narrower energy interval. In laser-driven beamlines this function is essential because the source does not provide a narrow therapeutic energy layer by itself. A two-dipole arrangement can also restore the selected trajectory toward the original axis, combining energy selection with compact geometrical alignment. [40-42, 44]

Quadrupole magnets provide transverse focusing through a magnetic field gradient. A single quadrupole focuses in one plane while defocusing in the perpendicular plane, so practical systems use doublets, triplets, or longer alternating sequences. Their focusing strength is proportional to the magnetic gradient and inversely proportional to particle momentum. This makes quadrupoles sensitive to energy spread: lower-energy particles are over-focused and higher-energy particles are under-focused. In a laser-driven beam, where energy spread is large, quadrupoles must therefore be used together with energy selection and careful matching. [40-42, 44-45]

Solenoids provide simultaneous focusing in both transverse planes and are especially useful near a divergent source. A particle entering an axial solenoidal field follows a helical trajectory, with a Larmor radius determined by transverse momentum and magnetic field. Strong axial fields reduce the radial excursion and can keep a divergent beam inside the aperture long enough to form a downstream waist. For laser-driven ion beams, this is valuable because the first transport stage is usually dominated by the need to capture particles before the envelope expands beyond the available bore. [40, 42-43, 45]

The solenoid is not simply a thin lens. Its focusing strength depends on the integral of the square of the axial field along the path, the particle species, charge state, kinetic energy, field map, and fringe fields. In finite coils, the entrance and exit fringe fields are part of the focusing system. When multiple solenoids are placed close together, fringe-field overlap increases the effective magnetic length and can improve confinement. This makes modular solenoid arrays attractive for early capture, especially when a single long high-field magnet would be expensive or mechanically difficult. [40, 42-43, 45]

The relevant beam quantities are beam size, divergence, phase-space distribution, emittance, envelope, transmission efficiency, and energy spread. Beam size and envelope determine whether particles remain inside apertures. Divergence determines how quickly the beam expands and how much early focusing is required. Emittance combines spatial and angular spread and indicates how easily the distribution can be focused. Transmission efficiency measures the fraction of particles preserved through a section. Energy spread controls chromatic effects and the strength of dispersive separation. [40-42, 44-45]

These quantities are coupled. A larger aperture can increase transmission but also increases magnet size, conductor requirements, cryogenic load, stored energy, and cost. Stronger focusing can reduce beam size but may increase chromatic aberrations or create losses if the beam is mismatched into downstream elements. A narrow slit can improve energy purity but reduces particle number. The design task is therefore not to maximize one parameter in isolation, but to preserve a useful particle population with acceptable energy selection, spatial confinement, and realistic magnet specifications. [40-42, 45]

4. Simulation Method and Magnet Design

The methodology follows a modular simulation workflow. Individual magnetic elements are first designed and evaluated separately, then combined into larger beamline sections and finally into an end-to-end transport line. This approach makes it possible to identify the role of each component and to understand where particle losses occur. The workflow begins with a particle source definition, continues with magnetic geometry and field calculation, then uses particle tracking to obtain trajectories, beam envelopes, phase-space plots, energy spectra, and transmission efficiencies.

Two simulation environments were used. SIMION 8.1 was applied to the proton beamline studies because it allows rapid particle-optics exploration with complex arrangements of magnetic elements, filters, slits, and detector planes. CST Studio Suite was used for ion transport because it provides three-dimensional magnetostatic field calculation and particle tracking through realistic field maps. OPERA field modelling was also used for dipole analysis. The combination of these tools allows both fast conceptual studies and more realistic field-map-based ion transport. [46-47]

The proton beamline is a compact steering and filtering system with a total length of 3864 mm. It includes two dipoles, a spatial mass filter, two quadrupole pairs, a final collimating filter, a slit, and a detector screen. The first dipole separates useful protons from unwanted secondary radiation, while the second dipole restores the selected trajectory. The quadrupoles provide alternating focusing, and the filters and slit reduce the transverse and spectral spread. The simulated proton source covers 70-130 MeV and is treated first with a simplified distribution and then with an inverse-exponential TNSA-like distribution. [46]

The ion transport line is more complex because carbon ions have higher magnetic rigidity and require stronger focusing. The line is divided into four functional stages: a high-field solenoid section for early capture, a first quadrupole triplet for transverse conditioning, a dipole semi-chicane for energy-dependent separation and species rejection, and a second quadrupole triplet for final focusing toward the irradiation plane. This architecture reflects the fact that no single element can solve the source problem. Capture, energy selection, and final focusing must be optimized as a coupled system. [40-41, 47]

The initial carbon-ion design is based on a 100 MeV/u fully stripped carbon beam emitted with a total angular divergence of 20 degrees, corresponding to a +/-10 degree half-angle. At 200 mm from the interaction point, simple geometric expansion gives a beam diameter of roughly 72 mm. An 80 mm inner solenoid diameter was therefore chosen as a practical baseline. This does not mean the full angular cone is captured. The high-field superconducting configuration accepts mainly the central angular core, with an approximate accepted half-angle of about +/-4.0 to +/-4.5 degrees for fields in the 11-12.5 T range. [40-42]

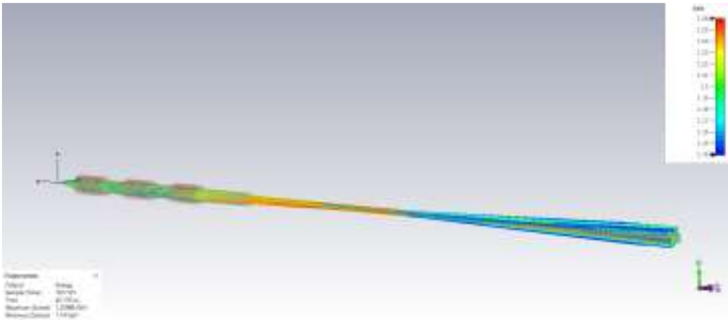

Fig. 1 – 3D trajectories of a 95-105 MeV/u carbon ion beam.

The aperture choice is a deliberate compromise. Increasing the bore improves acceptance of large-angle particles, but it also increases superconducting tape length, cryostat dimensions, stored energy, mechanical forces, and cost. A larger aperture can recover particles from the low-density halo, but it makes the magnet system heavier and more expensive. The 80 mm bore therefore prioritizes a transportable high-density core rather than complete capture of the full nominal laser-driven cone.

Pulsed normal-conducting solenoids were considered as a reference case because high-field pulsed solenoids have already been used in laser-driven ion transport experiments. A six-solenoid pulsed configuration with field overlap demonstrated the field scale needed for capture, reaching approximately 7 T per element and increasing the effective magnetic length through fringe-field superposition. This option is useful as a technological benchmark, but it requires high peak currents, pulsed-power synchronization, strong thermal management, and low-duty-cycle operation. It is not retained as the final design path. [40-41, 43]

The final capture concept uses high-temperature superconducting solenoids based on YBCO tape. Each solenoid has an effective inner radius of 46 mm, outer radius of 66 mm, and length of 240 mm. With a 12 mm wide and 0.1 mm thick tape, the estimated tape length is approximately 1407 m per solenoid, corresponding to roughly 4000 turns. At 600 A, the excitation reaches about 2.4 MA-turns per solenoid, consistent with an on-axis field of approximately 11 T. The optimized configuration uses three solenoids rather than six, reducing the estimated YBCO tape cost from roughly 634,000 euros to roughly 317,000 euros. [48]

The superconducting design is treated at specification level. The selected 600 A operating point lies below the nominal 800 A tape rating, but a complete construction design would require field-angle-dependent critical-current data, load-line analysis, quench protection, stored-energy extraction, cryogenic heat-load calculation, conductor layout, mechanical stress evaluation, and detailed manufacturing tolerances. The thesis therefore uses the HTS model to obtain realistic field maps for particle transport, not to claim that all superconducting engineering questions are closed. [48]

The first quadrupole triplet is placed after the solenoid waist, near 3002 mm from the source. Its role is not aggressive beam compression, but controlled transport and matching into the dispersive section. A focusing-defocusing-focusing layout is used because it provides an extra degree of freedom compared with a doublet and helps control beam roundness after solenoidal coupling. The design keeps gradients below 35 T/m, with the optimized specification around 13 T/m, 13 T/m, and 7 T/m for the three magnets in the first triplet.

The dipole semi-chicane is designed around the rigidity of the 100 MeV/u carbon reference beam, approximately 2.96 T m. In the selected 95-105 MeV/u interval, the rigidity varies from about 2.88 to 3.03 T m, a spread of roughly 5%. The dipoles use fields near 1 T and are arranged to create horizontal energy dispersion while allowing the selected trajectory to continue toward the downstream focusing section. The second triplet then uses a larger aperture and stronger gradients, about 21-22 T/m, to control the beam after the chicane and form the final irradiation-scale spot. [40-42, 44]

5. Proton Transport Studies

The proton simulations establish the first magnetic selection concept for a laser-driven beam. The initial beamline uses two dipoles to separate and redirect particles, quadrupoles to focus the accepted distribution, and filters and slits to shape the spatial and energy profile. The detector-plane results show that the magnetic elements displace the largest fraction of particles from the initial axis, as expected from the dispersive action of the dipoles. With only 5000 simulated particles, the raw spot is difficult to interpret in detail, but post-processing shows an approximately elliptical distribution with modest energy separation across the accepted region. [46]

The comparison between configurations without filtering, with one collimator, and with both collimator and slit shows the value of sequential beam conditioning. Each additional filtering stage improves the energy spectrum and the spatial uniformity at the detector, while reducing the delivered particle number. This trade-off is unavoidable in laser-driven beams. A broad source can be made cleaner only by rejecting part of the distribution. For radiobiology experiments, this loss can be acceptable if the remaining beam has a more reproducible position, energy interval, and transverse profile.

When the input distribution is changed to an inverse-exponential form, closer to a TNSA-like proton spectrum, the detector energy spectrum remains dominated by particles in the 80-90 MeV range under the same magnet settings. The lower transmitted count is consistent with the fact that most source particles occupy the lower 70-80 MeV interval and do not satisfy the same transport conditions. The spatial profile remains limited and oval, with most particles concentrated within roughly 6 mm in one transverse direction and 15 mm in the other. [16-17, 20]

The phase-space plots show additional structure because the source is not monoenergetic. The finite particle count also makes the distribution appear irregular. Expanding the data set synthetically from 5000 to 100000 particles clarifies the shape imposed by the final slit and reduces the visual effect of low statistics. This does not replace a high-statistics full simulation, but it helps interpret the optical behaviour of the selected geometry. The narrow outlier feature observed in the expanded set is treated as a simulation artifact rather than a physical beam component. [40-42, 45]

The proton study demonstrates the general principle that compact magnetic components can select and shape a laser-driven proton population. It also shows the limitations of the approach. Energy filtering improves beam definition but reduces flux. Quadrupole focusing remains sensitive to energy spread. A slit can make the spot more usable but cannot create source stability by itself. These lessons carry into the carbon-ion work, where the same transport logic must be applied under more difficult rigidity and aperture conditions.

6. Carbon and Helium Ion Transport

The carbon-ion simulations focus on the transport of a 95-105 MeV/u population through a compact line composed of high-field solenoids, quadrupole triplets, and a dipole semi-chicane. Carbon is more challenging than protons because its magnetic rigidity is substantially higher at comparable energy per nucleon. The solenoid section must therefore provide strong early focusing while accepting a beam that begins with large angular spread. Complete capture of the full source cone is not the design goal; the system is intended to preserve the useful central angular core. [4-5, 40-41]

The first solenoid simulations show that 100 MeV/u carbon ions are only partially captured by the 80 mm bore. This is expected. Large-angle particles intercept the bore before the magnetic field can rotate and confine their trajectories. The beam waist forms downstream of the solenoid assembly, close to 3002 mm from the source, and becomes the injection plane for the following quadrupole triplet. The focusing is weaker than for protons, which is consistent with the higher rigidity of carbon ions and confirms the need for high-field or multi-element capture. [40-42]

a) b)

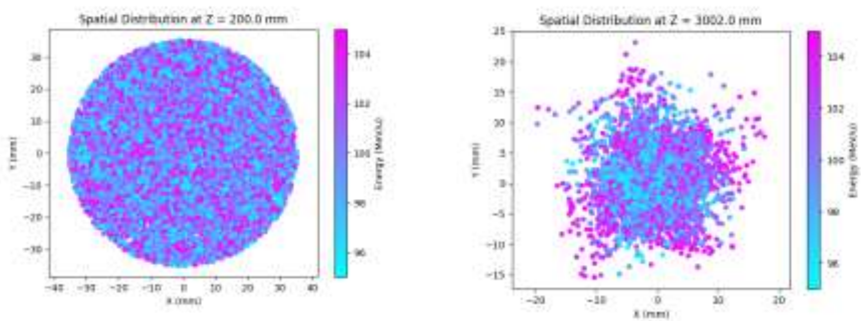

Fig. 2 - a) Spatial distribution at the entrance of the first solenoid, b) spatial distribution at the focal spot

Energy-dependent solenoid studies at 40, 60, and 100 MeV/u show that most losses occur in the first solenoid and near the entrance of the second. The transport is therefore angular-acceptance limited. Lower-energy particles are more strongly affected by the same magnetic field, while higher-energy particles are more difficult to bend and confine. When the initial divergence is increased from 10 degrees to 40 degrees, transmission drops because a growing fraction of particles enters outside the transportable angular range. The envelope plots confirm that low-divergence cases form cleaner downstream waists, while high-divergence cases suffer early clipping. [10, 16-17, 40, 42, 45]

Helium ions were simulated as an alternative light-ion species. From a first-order transport point of view, fully stripped helium and fully stripped carbon have the same mass-to-charge ratio. At the same kinetic energy per nucleon, their magnetic rigidities are therefore similar, and the same magnetic field maps produce comparable focusing. The helium results confirm this expectation. Their differences from carbon become more important for source production, target design, fragmentation, stopping power, and radiobiology than for the first-order magnetic optics considered in the transport line. [16-17, 40, 43]

The aperture study shows the cost-performance character of the solenoid design. Increasing the inner aperture from 80 mm to 100 mm improves transport efficiency by only about 8% in the estimate, while increasing superconducting material, cryostat size, stored energy, and mechanical complexity. This supports the decision to retain the 80 mm bore. The chosen system is not optimized for maximum possible particle capture; it is optimized for a useful transported core within a magnet envelope that remains plausible for an HTS implementation.

After optimization of the solenoid field, the transport of the 95-105 MeV/u carbon beam improves noticeably. The number of transported particles rises from approximately 3800 to about 5000 in the simulation, corresponding to a capture efficiency of 31.25%. At the focal plane, the spatial distribution changes from an approximately uniform entrance distribution to a more Gaussian-like core. Although the beam envelope can suggest a larger ring, most particles are concentrated in a central spot of roughly 28 mm diameter. This distinction between envelope and high-density core is important because beamline design should be based on the useful dose region, not only on the outermost particles.

The simulation of a broader 60-100 MeV/u carbon distribution highlights chromatic behaviour. Each energy bin has a different focal condition, and lower-energy particles are more strongly focused. The 60-70 MeV/u and 70-80 MeV/u bins remain more compact, while the 90-100 MeV/u bin expands more strongly. Across the whole spectrum, the beam envelope is larger than the high-density core, meaning that a physical aperture could select a more useful spatial and energy region. However, such selection must be coordinated with the required dose per pulse, because a TNSA-like spectrum contains fewer high-energy ions. [40-42, 44-45]

The first quadrupole triplet is used to prepare the solenoid output for the dipole chicane. Its optimized gradients, about 13 T/m, 13 T/m, and 7 T/m, keep the beam nearly parallel in the more important plane and shift the focus toward the interior of the semi-chicane. This improves transport through the dispersive section. The triplet results show nearly complete transmission in the baseline configuration, with losses below 0.2%, and about 82% of transmitted particles inside a 10 mm usable radius at the chosen exit plane. Combined with the entrance efficiency, the total usable fraction is about one quarter of the initial source population for that stage. [40-41, 47]

The dipole semi-chicane provides the main energy-selection function for carbon ions. OPERA tracking shows the expected rigidity-dependent deflection: as ion energy increases, the bending angle decreases. Representative exported trajectories decrease from about 27.7 degrees near 10 MeV/u to about 15.6 degrees at 100 MeV/u. This produces spatial separation between energy groups and allows a practical selection window in the 90-100 MeV/u or 95-105 MeV/u region. The result should be interpreted as qualitative-to-specification-level energy separation; a final experimental design would still require an explicit slit-plane table with centroids, RMS sizes, chosen slit width, and transmitted fractions. [40-42, 44]

The semi-chicane was optimized after an initial geometry caused a sharp transmission drop and particle impact on the second magnet yoke. The improved version reduces the longitudinal distance between dipoles, increases the gap from 30 mm to 40 mm, uses a 250 mm separation and 80 mm transverse offset, and rotates the dispersion into the horizontal plane. This orientation is more practical for slit placement, mechanical integration, and target positioning. The dipole fields are approximately 1.1 T in the first magnet and 1.0 T in the second, with the asymmetry compensating residual horizontal tilt.

After the optimized chicane, the residual horizontal divergence is small. The mean position difference between two downstream monitors separated by 60 mm is about 0.2 mm, corresponding to approximately 3.33 mrad or 0.191 degrees. This indicates that the reference direction is largely restored, although some residual spatial dispersion may remain. The high-energy carbon selection window is also separated from proton trajectories under the assumed source conditions, so the dipole system contributes to species rejection. It should not be read as absolute elimination of every possible contaminant, but as rigidity-based separation of the intended carbon interval.

The second quadrupole triplet is designed after evaluating the upstream beam at the chicane output. The beam is diverging mainly in one transverse direction, so the first quadrupole is oriented to focus that plane. A 70 mm aperture is selected because a 50 mm bore would place useful particles too close to nonlinear near-pole regions. The triplet uses gradients of approximately 21 T/m, 22 T/m, and 20 T/m. The iron approaches the onset of saturation near the pole region, identifying a design area for future refinement, but the field level remains useful for transport simulation. [40-41]

a) b)

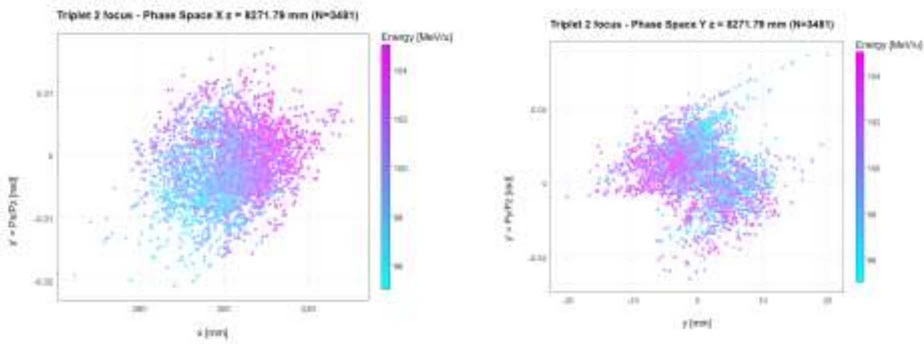

c)

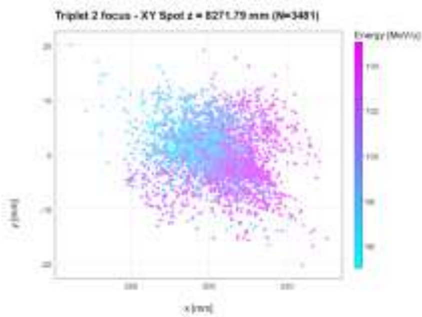

Fig. 3 – Focal Spot parameters of Triplet 2

The complete optimized carbon beamline begins with three HTS solenoids starting 200 mm from the source, followed by a first quadrupole triplet, a horizontal dipole semi-chicane, and a second triplet. The final focal spot is located approximately 8272 mm from the source and 1087 mm downstream of the last quadrupole. Most of the particle population is concentrated in an approximately 20 mm by 20 mm region, with a slight energy-dependent displacement. The spot is suitable for a radiobiology-scale irradiation geometry, but it is not yet a final clinical beam spot. [47]

The full carbon line reaches about 21.1% total transmission before final aperturing. Applying a 20 mm diameter accepted region reduces transmission to about 14.4%, but improves the spatial definition of the accepted beam. This is the central trade-off of the final stage: the aperture does not improve the beam for free, but converts part of the transported distribution into a more reproducible irradiation field. For controlled radiobiology, this may be preferable to a larger, less defined beam with higher particle count.

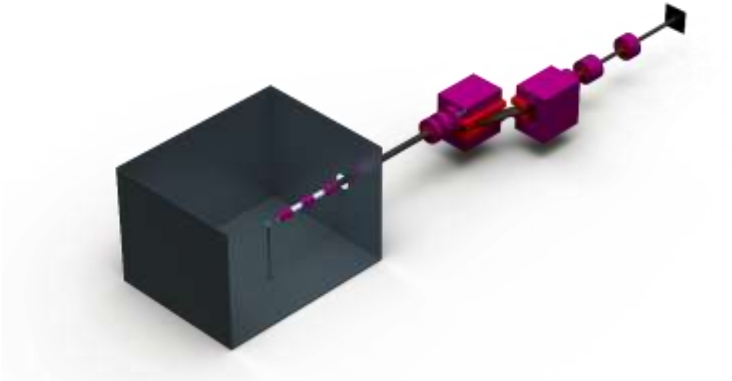

Fig. 4 – 3D render of the final transport

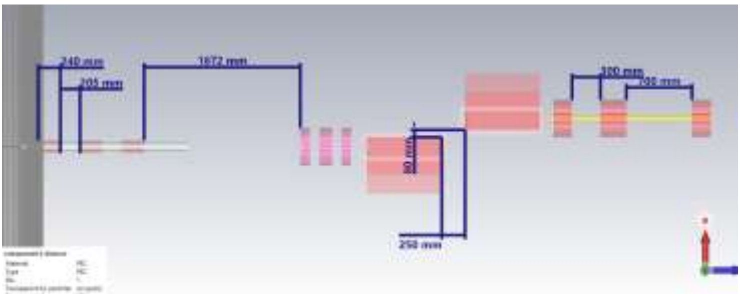

Fig. 5 – CST top view of the transport system

The helium simulation through the optimized full line gives very similar behaviour to carbon. The transported population changes only modestly, and the final focal position shifts from about 8272 mm for carbon to about 8317 mm for helium. This confirms that the line response is governed mainly by magnetic rigidity and mass-to-charge ratio. It also suggests that the same general magnetic architecture could support more than one light-ion species, provided that source production, energy spectrum, dose deposition, and radiobiological requirements are evaluated separately. [16-17, 40-42]

7. Dose Estimate, Discussion, and Contributions

The final beamline must be judged not only by transmission, but also by the dose-relevant properties of the selected ion population. SRIM simulations were used to estimate the ionization behaviour of carbon ions in water across the 95-105 MeV/u interval. The calculated Bragg band extends from approximately 23.3 mm to 29.5 mm in water, with maximum local ionization close to 18 eV per Angstrom per ion. For dose estimation, the work uses an average over the Bragg-band region rather than assuming that all energy is deposited at a single point. [7]

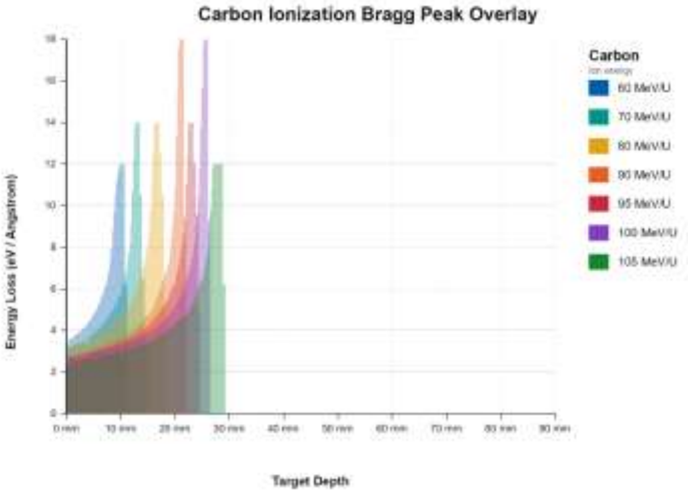

Fig. 6 – Bragg Peaks for carbon ions in waterx

The combined Bragg-band LET is obtained from the 95, 100, and 105 MeV/u curves using Simpson weighting and then averaged over the finite depth interval. This gives an average value of about 6.1633 eV per Angstrom per ion across the Bragg band. The focal-plane particle distribution is taken as approximately 40 mm by 20 mm, corresponding to an area of 8 cm2. The transport efficiency is taken from the CST results, with 0.213 for the unaperturized Triplet 2 focus and 0.1444 for the aperturized focus. [7, 47]

For 1e8 initial ions, the unaperturized case delivers approximately 0.263 Gy across the Bragg-band estimate, while the aperturized case delivers approximately 0.178 Gy. The number of initial ions required for 1 Gy per pulse is therefore about 3.81e8 without the final aperture and 5.61e8 with the aperture. Using a focal arrival-time width of 2.466 ns, the corresponding instantaneous in-pulse dose rates are on the order of 1e8 Gy/s. These values are relevant to FLASH-like dose-rate conditions, while still depending on source yield, selected bandwidth, focal area, and transmission. [25-28, 31]

Case	**Dose region**	**Dose per 1e8 initial ions**	**Initial ions for 1 Gy (averaged over Bragg Band)**	**Dose rate for 1e8 ions**
No aperture	Whole Bragg band, 40 mm x 20 mm	0.263 Gy	3.81e8	1.06e8 Gy/s
Aperturized	Whole Bragg band, 40 mm x 20 mm	0.178 Gy	5.61e8	7.23e7 Gy/s

Table 1 – Calculated necessary total particle number to achieve 1 Gy

The dose estimate shows why laser-driven carbon ions are attractive and difficult at the same time. A sufficiently intense pulse can in principle deliver biologically relevant dose at extremely high instantaneous dose rate, but the useful dose depends on how many ions survive capture, selection, and final focusing. Aperturing improves spatial reproducibility but increases the source yield required for the same dose. A clean beam with too few particles is not useful; a high-flux beam with poor spatial and energy control is also not useful. The transport line must therefore be optimized for dose delivery, energy bandwidth, halo suppression, and reproducibility together. [7, 25-28, 31, 47]

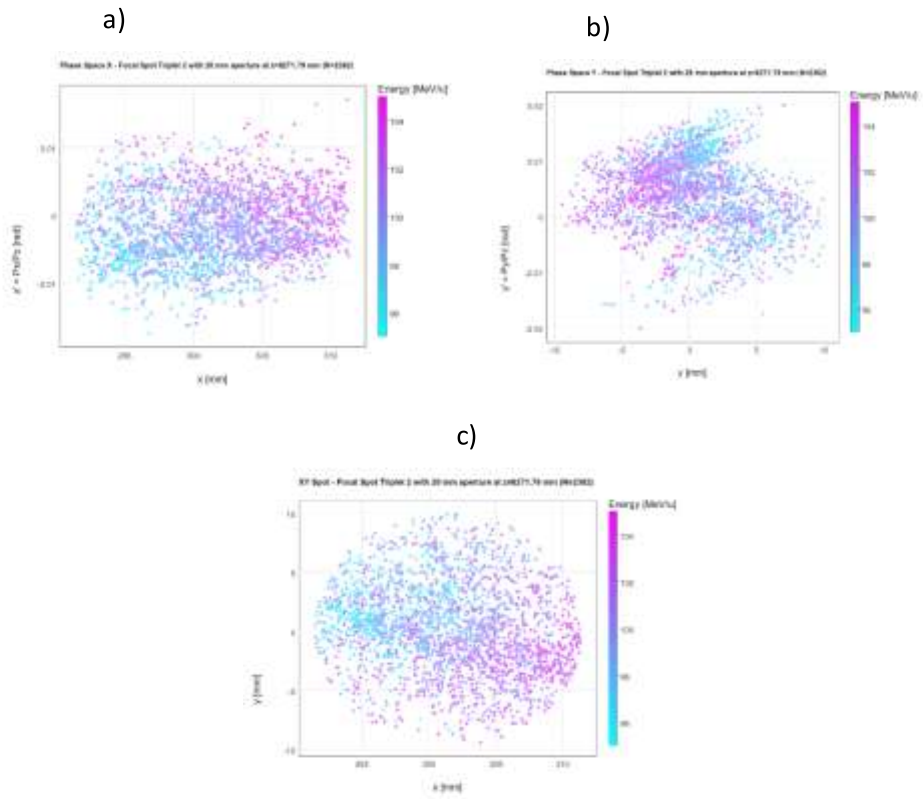

Fig. 7 - Aperturized focal spot parameters - a) XX’ phase space, b) YY’ phase space, c) XY spot

The final configuration demonstrates a realistic baseline for compact magnetic transport of laser-driven carbon ions in the selected energy interval. It does not represent a complete clinical treatment system. The simulated magnets are realistic at specification level, but detailed engineering remains necessary before construction. The HTS solenoids require critical-current validation under field, temperature, angle, and strain; cryogenic and quench-protection systems must be designed; quadrupole pole shapes and field quality must be optimized; dipole fringe fields and slit-plane transmission must be measured or modelled in greater detail. [48]

The beamline also requires additional diagnostics and correction in a future experimental version. Beam-position monitors, scintillator screens, time-of-flight diagnostics, dose monitors, and small steering correctors would be needed to tune the line shot by shot and to compensate residual alignment errors. Additional quadrupole stages after the energy-selection section could reduce the final spot size, improve symmetry, and suppress halo. Slit optimization should be performed with explicit dose requirements, because narrowing the selected energy interval reduces particle flux.

The main scientific contribution is the connection between laser-plasma source conditions and realistic magnetic transport requirements for hadron-therapy-related ion beams. The work shows that high-field solenoids are essential for early capture, that aperture selection is a cost-performance decision, and that carbon-ion transport is governed by magnetic rigidity, divergence, and chromatic effects. It also shows that a complete line must combine solenoids, quadrupoles, and a dipole semi-chicane rather than relying on a single focusing element. [10, 18-19, 40, 42, 45]

A second contribution is the specification-level comparison between pulsed copper and HTS solenoid operation. Pulsed copper can reach high fields and is useful for low-duty-cycle experiments, but repeated radiobiological irradiation favours superconducting operation if the engineering constraints can be solved. The three-solenoid HTS layout reduces material cost relative to a six-solenoid version while preserving sufficient focusing strength for the selected carbon core. This provides a more plausible baseline for repeated-use beamline development. [48]

A third contribution is the integration of transport simulations with dose-relevant SRIM estimates. The selected 95-105 MeV/u carbon population is not evaluated only as a set of trajectories, but also as a particle distribution capable of producing a Bragg band in water and a pulse dose under defined assumptions. This connects magnetic design to the medical-physics motivation of the work. The resulting dose-rate estimate is not a clinical claim, but it shows that the transported population can reach a regime relevant to ultra-high-dose-rate radiobiology if the source yield is sufficient. [7, 25-28, 31]

Overall, laser-driven ion acceleration remains a promising but technically demanding route toward compact hadron-therapy systems. The acceleration mechanism is compact and naturally produces ultra-short bunches, but clinical translation depends on source stability, energy control, repetition rate, transport efficiency, dosimetry, and biological validation. The present work establishes a feasible magnetic-transport baseline for laser-driven carbon ions, identifies the principal loss mechanisms, and defines the next engineering and experimental steps needed before such beams can move from conceptual feasibility toward clinically meaningful application. [10, 16-19, 25-31]

References

[1] R. R. Wilson, "Radiological use of fast protons," Radiology, 1946. doi: 10.1148/47.5.487.

[2] M. Durante, J. S. Loeffler, "Charged particles in radiation oncology," Nature Reviews Clinical Oncology, 2010. doi: 10.1038/nrclinonc.2009.183.

[3] G. Kraft, "Tumor therapy with heavy charged particles," Progress in Particle and Nuclear Physics, 2000. doi: 10.1016/S0146-6410(00)00112-5.

[4] H. Paganetti, Proton Therapy Physics, 2025. doi: 10.1201/9781032616858.

[5] U. Amaldi, G. Kraft, "Radiotherapy with beams of carbon ions," Reports on Progress in Physics, 2005. doi: 10.1088/0034-4885/68/8/R04.

[6] ICRU, "ICRU Report 49, Stopping Power and Ranges for Protons and Alpha Particles."

[7] J. F. Ziegler, M. D. Ziegler, J. P. Biersack, "SRIM - The stopping and range of ions in matter (2010)," Nuclear Instruments and Methods in Physics Research Section B, 2010. doi: 10.1016/j.nimb.2010.02.091.

[8] A. J. Lomax, "Intensity modulated proton therapy and its sensitivity to treatment uncertainties 1: the potential effects of calculational uncertainties," Physics in Medicine and Biology, 2008. doi: 10.1088/0031-9155/53/4/014.

[9] E. Pedroni, R. Bacher, H. Blattmann, T. Bohringer, A. Coray, A. Lomax, et al., "The 200-MeV proton therapy

project at the Paul Scherrer Institute: conceptual design and practical realization," Medical Physics, 1995. doi: 10.1118/1.597522.

[10] S. V. Bulanov, T. Z. Esirkepov, V. S. Khoroshkov, A. V. Kuznetsov, F. Pegoraro, "Oncological hadrontherapy with laser ion accelerators," Physics Letters A, 2002. doi: 10.1016/S0375-9601(02)00521-2.

[11] D. Strickland, G. Mourou, "Compression of amplified chirped optical pulses," Optics Communications, 1985. doi: 10.1016/0030-4018(85)90120-8.

[12] C. Danson, C. Haefner, J. Bromage, T. Butcher, J.-C. Chanteloup, E. Chowdhury, et al., "Petawatt and exawatt class lasers worldwide," High Power Laser Science and Engineering, 2019. doi: 10.1017/hpl.2019.36.

[13] C. Radier, O. Chalus, M. Charbonneau, S. Thambirajah, G. Deschamps, S. David, et al., "10 PW peak power femtosecond laser pulses at ELI-NP," High Power Laser Science and Engineering, 2022. doi: 10.1017/hpl.2022.11.

[14] S. Gales, K. A. Tanaka, D. L. Balabanski, F. Negoita, D. Stutman, O. Tesileanu, et al., "The extreme light infrastructure-nuclear physics (ELI-NP) facility: new horizons in physics with 10 PW ultra-intense lasers and 20 MeV brilliant gamma beams," Reports on Progress in Physics, 2018. doi: 10.1088/1361-6633/aacfe8.

[15] S. Wilks, A. B. Langdon, T. Cowan, M. Roth, M. Singh, S. Hatchett, et al., "Energetic Proton Generation in Ultra-Intense Laser-solid Interactions," Physics of Plasmas, 2001. doi: 10.1063/1.1333697.

[16] H. Daido, M. Nishiuchi, A. S. Pirozhkov, "Review of laser-driven ion sources and their applications," Reports on Progress in Physics, 2012. doi: 10.1088/0034-4885/75/5/056401.

[17] A. Macchi, M. Borghesi, M. Passoni, "Ion acceleration by superintense laser-plasma interaction," Reviews of Modern Physics, 2013. doi: 10.1103/RevModPhys.85.751.

[18] E. Fourkal, J. S. Li, M. Ding, T. Tajima, C.-M. Ma, "Particle selection for laser-accelerated proton therapy feasibility study," Medical Physics, 2003. doi: 10.1118/1.1586268.

[19] L. Pommarel, B. Vauzour, F. Megnin-Chanet, E. Bayart, O. Delmas, F. Goudjil, et al., "Spectral and spatial shaping of a laser-produced ion beam for radiation-biology experiments," Physical Review Accelerators and Beams, 2017. doi: 10.1103/PhysRevAccelBeams.20.032801.

[20] M. Roth, M. Schollmeier, "Ion Acceleration-Target Normal Sheath Acceleration," CERN Yellow Reports, 2016. doi: 10.5170/CERN-2016-001.231.

[21] W. Kruer, The Physics Of Laser Plasma Interactions, 2019.

[22] P. Gibbon, "Short Pulse Laser Interactions with Matter: An Introduction," 2005. doi: 10.1142/P116.

[23] L. Yin, B. J. Albright, B. M. Hegelich, and J. C. Fernandez, "GeV laser ion acceleration from ultrathin targets: The laser break-out afterburner," Laser and Particle Beams, vol. 24, no. 2, pp. 291-298, 2006. doi: 10.1017/S0263034606060459.

[24] L. Yin, B. J. Albright, B. M. Hegelich, K. J. Bowers, K. A. Flippo, T. J. T. Kwan, and J. C. Fernandez, "Monoenergetic and GeV ion acceleration from the laser breakout afterburner using ultrathin targets," Physics of Plasmas, vol. 14, 056706, 2007. doi: 10.1063/1.2436857.

[25] V. Favaudon, L. Caplier, V. Monceau, F. Pouzoulet, M. Sayarath, C. Fouillade, et al., "Ultrahigh dose-rate FLASH irradiation increases the differential response between normal and tumor tissue in mice," Science Translational Medicine, 2014. doi: 10.1126/scitranslmed.3008973.

[26] Y. Alaghband, S. N. Cheeks, B. D. Allen, P. Montay-Gruel, N.-L. Doan, B. Petit, et al., "Neuroprotection of Radiosensitive Juvenile Mice by Ultra-High Dose Rate FLASH Irradiation," Cancers, 2020. doi: 10.3390/cancers12061671.

[27] P. Montay-Gruel, M. M. Acharya, K. Petersson, L. Alikhani, C. Yakkala, B. D. Allen, et al., "Long-term neurocognitive benefits of FLASH radiotherapy driven by reduced reactive oxygen species," Proceedings of the National Academy of Sciences, 2019. doi: 10.1073/pnas.1901777116.

[28] J. D. Wilson, E. M. Hammond, G. S. Higgins, K. Petersson, "Ultra-High Dose Rate (FLASH) Radiotherapy: Silver Bullet or Fool's Gold?," Frontiers in Oncology, 2020. doi: 10.3389/fonc.2019.01563.

[29] P. Chaudhary, G. Milluzzo, H. Ahmed, B. Odlozilik, A. McMurray, K. M. Prise, et al., "Radiobiology Experiments With Ultra-high Dose Rate Laser-Driven Protons:

Methodology and State-of-the-Art," Frontiers in Physics, 2021. doi: 10.3389/fphy.2021.624963.

[30] A. Flacco, E. Bayart, L. Romagnani, M. Cavallone, L. De Marzi, C. Fouillade, et al., "Laser driven FLASH radiobiology using a high dose and ultra high dose rate single pulse proton source," Scientific Reports, 2025. doi: 10.1038/s41598-025-01105-z.

[31] M.-C. Vozenin, J. Bourhis, M. Durante, "Towards clinical translation of FLASH radiotherapy," Nature Reviews Clinical Oncology, 2022. doi: 10.1038/s41571-022-00697-z.

[32] J. Bourhis, W. Jeanneret Sozzi, P. Goncalves Jorge, O. Gaide, C. Bailat, F. Duclos, et al., "Treatment of a first patient with FLASH-radiotherapy," Radiotherapy and Oncology, 2019. doi: 10.1016/j.radonc.2019.06.019.

[33] A. E. Mascia, E. C. Daugherty, Y. Zhang, E. Lee, Z. Xiao, M. Sertorio, et al., "Proton FLASH Radiotherapy for the Treatment of Symptomatic Bone Metastases: The FAST-01 Nonrandomized Trial," JAMA Oncology, 2023. doi: 10.1001/jamaoncol.2022.5843.

[34] E. C. Daugherty, Y. Zhang, Z. Xiao, A. E. Mascia, M. Sertorio, J. Woo, et al., "FLASH radiotherapy for the treatment of symptomatic bone metastases in the thorax (FAST-02): protocol for a prospective study of a novel radiotherapy approach," Radiation Oncology, 2024. doi: 10.1186/s13014-024-02419-4.

[35] S. Raschke, S. Spickermann, T. Toncian, M. Swantusch, J. Boeker, U. Giesen, et al., "Ultra-short laser-accelerated proton pulses have similar DNA-damaging effectiveness but

produce less immediate nitroxidative stress than conventional proton beams," Scientific Reports, 2016. doi: 10.1038/srep32441.

[36] K. Zeil, M. Baumann, E. Beyreuther, T. Burris-Mog, T. E. Cowan, W. Enghardt, et al., "Dose-controlled irradiation of cancer cells with laser-accelerated proton pulses," Applied Physics B, 2013. doi: 10.1007/s00340-012-5275-3.

[37] S. D. Kraft, C. Richter, K. Zeil, M. Baumann, E. Beyreuther, S. Bock, et al., "Dose-dependent biological damage of tumour cells by laser-accelerated proton beams," New Journal of Physics, 2010. doi: 10.1088/1367-2630/12/8/085003.

[38] E. Bayart, A. Flacco, O. Delmas, L. Pommarel, D. Levy, M. Cavallone, et al., "Fast dose fractionation using ultra-short laser accelerated proton pulses can increase cancer cell mortality, which relies on functional PARP1 protein," Scientific Reports, 2019. doi: 10.1038/s41598-019-46512-1.

[39] S. Rudigkeit, T. E. Schmid, A. C. Dombrowsky, J. Stolz, S. Bartzsch, C.-B. Chen, et al., "Proton-FLASH: effects of ultra-high dose rate irradiation on an in-vivo mouse ear model," Scientific Reports, 2024. doi: 10.1038/s41598-024-51951-6.

[40] H. Wiedemann, Particle accelerator physics: Third edition, 2007. doi: 10.1007/978-3-540-49045-6.

[41] A. Wolski, Beam Dynamics in High Energy Particle Accelerators, 2014. doi: 10.1142/P899.

[42] S.-Y. Lee, Accelerator Physics (Fourth Edition), 2018. doi: 10.1142/11111.

[43] J. D. Jackson, Classical Electrodynamics.

[44] B. Holzer, "Beam optics and lattice design for particle accelerators," 2013. doi: 10.48550/arXiv.1303.6514.

[45] M. Reiser, P. O'Shea, S. Bernal, R. Kishek, Theory and Design of Charged Particle Beams: Second Edition, 2008. doi: 10.1002/9783527622047.

[46] D. A. Dahl, "SIMION for the personal computer in reflection," International Journal of Mass Spectrometry, 2000. doi: 10.1016/S1387-3806(00)00305-5.

[47] Dassault Systemes, "CST Studio Suite: Electromagnetic Field Simulation Software," SIMULIA, 2026. Available: https://www.3ds.com/products/simulia/cst-studio-suite (accessed Apr. 21, 2026).

[48] H. S. Ruiz, J. Hanisch, M. Polichetti, A. Galluzzi, L. Gozzelino, D. Torsello, et al., "Critical current density in advanced superconductors," Progress in Materials Science, 2026. doi: 10.1016/j.pmatsci.2025.101492.